



Full Length Article

Crystal structure, phase transitions, and thermodynamic properties of magnesium metavanadate (MgV_2O_6)

Guishang Pei^{a,b}, Cheng Pan^c, Dapeng Zhong^{a,b}, Junyi Xiang^{a,b}, Xuewei Lv^{a,b,*}

^a College of Materials Science and Engineering, Chongqing University, Chongqing 400044, China

^b Chongqing Key Laboratory of Vanadium-Titanium Metallurgy and Advanced Materials, Chongqing University, Chongqing 400044, China

^c Pangang Group Research Institute Co., Ltd., Panzhihua 617000, China

Received 22 September 2021; received in revised form 23 April 2022; accepted 18 May 2022

Available online xxx

Abstract

As a promising anode material for magnesium ion rechargeable batteries, magnesium metavanadate (MgV_2O_6) has attracted considerable research interest in recent years. A MgV_2O_6 sample was synthesized via a facile solid-state reaction by multistep-firing stoichiometric mixtures of MgO and V_2O_5 powder under an air atmosphere. The solid-state phase transition from α - MgV_2O_6 to β - MgV_2O_6 occurred at 841 K and the enthalpy change was 4.37 ± 0.04 kJ/mol. The endothermic effect at 1014 K and the enthalpy change was 26.54 ± 0.26 kJ/mol, which is related to the incongruent melting of β - MgV_2O_6 . *In situ* XRD was performed to investigate phase transition of the as-prepared MgV_2O_6 at high temperatures. The cell parameters obtained by Rietveld refinement indicated that it crystallizes in a monoclinic system with the $C2/m$ space group, and the lattice parameters of $a = 9.280$ Å, $b = 3.501$ Å, $c = 6.731$ Å, $\beta = 111.76^\circ$. The solid-state phase transition from α - MgV_2O_6 to β - MgV_2O_6 was further studied by thermal kinetics, indicating that this process is controlled first by a fibril-like mechanism and then by a spherulitic-type mechanism with an increasing heating rate. Additionally, the enthalpy change of MgV_2O_6 at high temperatures was measured utilizing the drop calorimetry, heat capacity was calculated and given as: $C_p = 208.3 + 0.03583T - 4809000T^{-2}$ (298 – 923 K) ($\text{J mol}^{-1} \text{K}^{-1}$), the high-temperature heat capacity can be used to calculate Gibbs free energy of MgV_2O_6 at high temperatures.

© 2022 Chongqing University. Publishing services provided by Elsevier B.V. on behalf of KeAi Communications Co. Ltd.

This is an open access article under the CC BY-NC-ND license (<http://creativecommons.org/licenses/by-nc-nd/4.0/>)

Peer review under responsibility of Chongqing University

Keywords: MgV_2O_6 ; Crystal structure; Phase transitions; Thermodynamic functions.

1. Introduction

Rapid industrialization has aggravated present energy challenges, which in turn have greatly stimulated the development of lithium-ion rechargeable batteries (LIBs). In recent years, LIBs have been widely applied in portable electronic devices, such as mobile phones, laptop computers, digital cameras, and power tools, owing to their excellent performance which includes high power and energy density, elongated life cycle, and safety [1–3]. High-energy-density anode materials for LIBs are increasingly required to fulfill the growing demand for portable energy sources. Traditionally, graphite has been

applied as an anode material in commercial LIBs; however, it cannot meet the needs of large-scale batteries because of its low voltage, low specific capacity, and poor cyclability [4,5]. Thus, the exploration of the next-generation anode materials with high specific capacity and remarkable cyclic stability is urgently needed. The rechargeable magnesium battery may be an ideal candidate for high energy density batteries because of its natural abundance, comparatively low price of its raw materials, and the improved safety of batteries, as compared to lithium [6–15]. Among them, magnesium metavanadate (MgV_2O_6), the most promising candidate anode material for magnesium-ion rechargeable batteries, has attracted considerable research interest in recent years. Wang et al. [16] experimentally confirmed which nanobelt exhibited a high capacity of 425.7 mAh g^{-1} (at 0.2 A g^{-1}), outstanding rate capability (182.1 mAh g^{-1} at 10 A g^{-1}), and an ultra-stable

* Corresponding author at: College of Materials Science and Engineering, Chongqing University, Chongqing 400044, China.

E-mail address: lvxuewei@163.com (X. Lv).

<https://doi.org/10.1016/j.jma.2022.05.011>

2213-9567/© 2022 Chongqing University. Publishing services provided by Elsevier B.V. on behalf of KeAi Communications Co. Ltd. This is an open access article under the CC BY-NC-ND license (<http://creativecommons.org/licenses/by-nc-nd/4.0/>) Peer review under responsibility of Chongqing University

cycle without any visible deterioration up to 1500 cycles at 4 A g⁻¹.

To accelerate large-scale commercial applications and better understand the thermodynamic conditions of MgV₂O₆ and its service performance when utilized as anode materials in rechargeable magnesium batteries, a thorough knowledge of its structure, phase transitions, and thermodynamic properties, such as heat capacity, entropy, enthalpy, and Gibbs free energy, are indispensable [17,18]. The initial structural determination of MgV₂O₆ at room temperature was first reported by Gondrand et al. in 1974 [19]. Thereafter, Tang et al. [20] synthesized MgV₂O₆ powder by a high-pressure and high-temperature route, and comprehensively studied the detailed physical properties of orthorhombic MgV₂O₆ under high pressure using Raman spectroscopy at room temperature. In 2018, Rahman et al. [21] investigated the physical properties of the high-pressure polymorphism of MgV₂O₆ with the density functional theory. Although numerous experimental studies and theoretical calculations have been performed on MgV₂O₆, it is evident that the high-temperature phase of MgV₂O₆ and its transition mechanism are not yet structurally characterized.

Thermodynamically, heat capacity is one of the most fundamental thermal properties of materials and plays an important role in heat transfer, thermodynamic calculations, and the anharmonic property of lattice vibration. Khodos et al. [22] measured the heat capacity of MgV₂O₆ and calculated the entropy of formation at 298.15 K. All available high-temperature heat capacity data are only estimated values, which were obtained using the Neumann-Kopp rule [23,24]. Many calorimetric results confirmed that the estimated heat capacity values of mixed oxides are not sufficiently precise and reliable, especially in the high-temperature region [25,26]. However, experimental data on the high-temperature heat capacity of MgV₂O₆ is still lacking in the literature and known thermodynamic databases, such as FactSage[®], Thermal-Calc[®], HSC[®], and MTDATA[®].

This study aims to investigate the crystal structure, phase transitions, and thermodynamic properties of MgV₂O₆ at high temperatures. The MgV₂O₆ was first synthesized through a facile solid-state sintering process and was then characterized by X-ray diffraction (XRD), scanning electron microscopy (SEM), Fourier transform infrared spectroscopy (FTIR), and differential scanning calorimetry (DSC). Enthalpy change of the MgV₂O₆ at 298–923 K was measured by drop calorimetry and heat capacity was calculated.

2. Experimental

2.1. Sample preparation

Magnesium oxide (MgO) and vanadium pentoxide (V₂O₅), exceeding 99.99% and 99.95% purity, respectively, were used as the raw materials. Both precursors were supplied by Lian-shuo Biological Technology Co., Ltd., Shanghai, China. The raw oxide powders were roasted at 573 K under an air atmosphere for 5 h before weighing to eliminate any absorbed moisture and other impurities. Subsequently, MgV₂O₆ powder

was synthesized by roasting and milling according to a specific molar ratio of 1:1. The homogenous mixtures were compacted into pellets using a hydraulic press, sintered at the target temperature (873 K), maintained for 20 h under an air atmosphere, and were then subsequently cooled down to room temperature in the furnace. The roasted samples were pulverized in a vibration mill and roasted after pressing to form pellets. High-purity MgV₂O₆ samples were finally obtained by repeating the roasting and milling process five times.

2.2. Sample characterization

2.2.1. XRD

To determine the phase composition of the as-prepared MgV₂O₆ powder, qualitative and quantitative analyses were performed using powder XRD (PANalytical X'Pert Powder, Panalytical B.V.) with Cu-K α radiation ($\lambda = 0.154$ nm, 40 kV, and 75 mA) at an angular range of 10°–80° with a relatively slow scanning step of 0.01°/min at a given temperature. The diffraction locations and intensities of the samples were then analyzed with the Highscore Plus[®] 8.5 software package. Rietveld refinement was performed to determine the cell parameters of the as-prepared MgV₂O₆ powder. The phase structure of MgV₂O₆ at various temperatures was detected by *in situ* XRD. The powder sample was first dissolved in alcohol and then placed in a Pt flakelet to perform the experimental test at high temperature with a temperature step of 100 K.

2.2.2. FTIR

FTIR (Spectrum 100, PerkinElmer) was used to obtain the FTIR transmission spectrum of the MgV₂O₆ sample. An impedance analyzer was used to measure the frequency-dependent AC conductance, impedance, dielectric constant, capacitance, inductance, and reactance.

2.2.3. SEM

SEM (TESCANVEGA 3 LMH, Czech Republic) was also performed to further investigate the surface morphology and particle size of the MgV₂O₆ sample.

2.2.4. DSC

The enthalpy change and transition temperatures of the solid-state phase transformation and incongruent melting of MgV₂O₆ were measured by DSC, which was conducted on a NETZSCH DSC 404 F3 Pegasus thermal analyzer at temperatures ranging from room temperature to 1173 K at a specific heating rate of 10 K/min under an argon atmosphere and with an argon gas flow rate of 50 mL/min. The maximum temperature measurement uncertainty of the DSC instrument was ± 0.5 K and the enthalpy change uncertainty was $\pm 2.0\%$, which was established by determining that of the standard materials, namely, aluminum (99.999%, 12 ± 1 mg), zinc (99.999%, 12 ± 1 mg), tin (99.999%, 12 ± 1 mg), and indium (99.999%, 12 ± 1 mg). The experimental error was obtained by comparing the experimentally measured average and the standard values.

2.2.5. Drop calorimetry

The enthalpy increments of MgV_2O_6 powder at high temperatures were measured using an isothermal MHTC 96 line drop calorimeter (SETARAM, France). Calorimetric experiments were performed in flowing helium with a purity exceeding 99.999%. The measurements were conducted with a SETARAM drop sensor using sapphire ($\alpha\text{-Al}_2\text{O}_3$) as the standard reference material. The experimental principle of drop calorimetry is the measurement of the enthalpy increments of room temperature sample pellets which are dropped into the detector, which is maintained at a higher temperature. When a room-temperature sample pellet is dropped into the even temperature zone of the furnace, the additional heat content must be added to the system to maintain the programmed setting temperature. This heat content is proportional to the enthalpy increase of the sample at a specific temperature under normal pressure. The final MgV_2O_6 samples were post-treated to four small cubic samples with a mass of 80–100 mg for measurement. The room temperature samples were dropped into an alumina crucible in the furnace, which did not react with the sample powder below 973 K. The details of the calorimetric measurements and basic principles are described elsewhere [17].

The applicability and reliability of the MHTC 96 line were confirmed by heat capacity measurements of nickel (99.999%) with the drop module at temperatures from 373 to 873 K. $\alpha\text{-Al}_2\text{O}_3$ was used as the standard reference material. The deviations of the experimental results from those of the standard values were $\pm 2.0\%$ during the experimental interval, as compared to the values given by the former National Bureau of Standards [27]. Three specific temperature experiments of the MgV_2O_6 (673, 723, and 973 K) were conducted to verify the reliability and repeatability of the calorimetric process. The MgV_2O_6 heat capacity measurement error did not exceed 2.0, 2.0, and 1.5% at the specific temperatures, respectively.

3. Results and discussion

3.1. Synthesis and characterization

The thermodynamic feasibility of the specific chemical reaction is completely dependent on the values of the Gibbs free energy variation (ΔG) at a certain temperature. Assuming that the pressure is constant (1 atm), the chemical reaction can occur spontaneously at a specific temperature when the ΔG value is negative. The generation reaction of MgV_2O_6 is presented in Eq. (1) :



The ΔG of the MgV_2O_6 generation reaction with relationship to temperature was calculated using the Reaction module of the FactSage[®] software, and the results are presented in Fig. 1. The fundamental thermodynamic data of V_2O_5 , MgO , and MgV_2O_6 were extracted from literature [28], it should be noted that the oxide reference was used concerning standard enthalpy of formation, and entropy at 298.15 K, the results show in Table 1. Fig. 1 shows that the ΔG of the formation re-

action was negative when the temperature ranged from 298 to 1273 K, which confirmed that this reaction is thermodynamically feasible. The ΔG of the formation reaction markedly increased above 963 K, which may be caused by the melting of V_2O_5 . Although the formation of MgV_2O_6 is thermodynamically possible, the actual process is generally limited by dynamic conditions, such as diffusion and the rate of interfacial chemical reactions. Consequently, the temperature of the MgV_2O_6 generation reaction was set at 873 K through the comprehensive consideration of the V_2O_5 volatilization and the thermodynamic and kinetic aspects of the solid-state reaction.

X-ray powder diffraction was performed to detect the phase components and crystal structures of the as-prepared MgV_2O_6 sample at room temperature. Fig. 2 shows the experimental and Rietveld refinement results. The X-ray diffraction results show that the single-phase MgV_2O_6 sample was finally obtained using several roasting and milling processes. The sample is a single-phase, and the four main peaks which appear in the diffractograms correspond to the (0 0 1), (2 0 -1), (2 0 -2), and (1 1 -1) Bragg reflections of the MgV_2O_6 phase (ICDD card No: 95-152-2588). No excess peaks related to the starting materials or secondary phases, including other magnesium vanadate compounds such as $\text{Mg}_2\text{V}_2\text{O}_7$ and $\text{Mg}_3\text{V}_2\text{O}_8$, were detected in the 2θ range of 10–80°. A quantitative analysis using Highscore Plus[®] 8.5 indicated that the mass percent content of the prepared MgV_2O_6 sample exceeded 99.5%. The cell parameters obtained by the Rietveld refinement indicated that MgV_2O_6 was crystallized in the monoclinic system with space group $C2/m$, and the lattice parameters of $a = 9.280 \text{ \AA}$, $b = 3.501 \text{ \AA}$, $c = 6.731 \text{ \AA}$, $\beta = 111.76^\circ$. By comparing the experimental XRD patterns and the calculated patterns, the R_{wp} is 7.44702%, which means that the refinement results were acceptable.

The intensity ratio of the highest peak and the second highest peak indicates the highest degree of anion order in the crystal structure of the as-prepared MgV_2O_6 . The predominant peak and the second highest peak are 15,438 and 10,923, corresponding to the (1 1 -1) and (0 0 1) crystal faces, respectively, and yield an intensity ratio of 1.41. The intensity ratio values of the MgV_2O_6 sample were larger than the critical value of 1.2, which verifies that the as-prepared MgV_2O_6 powder exhibits good crystallinity.

Nanoscale crystal structures are usually formed during low-temperature ($< 1273 \text{ K}$) synthesis, which is not suitable for calorimetric measurements because of the uncertain impact of the surface contribution on the high-temperature heat capacity values [29]. Therefore, the average grain size of the final product was estimated using Scherrer's formula, the XRD instrument background was deduced, and a standard sample with a grain size of 5–20 μm was tested to correct the instrumental peak broadening term. The average grain size (D) of the MgV_2O_6 was estimated as follows:

$$D = K\lambda / \beta \cos\theta \quad (2)$$

where λ is the wavelength of the X-ray using $\text{Cu-K}\alpha$ radiation, K is the shape factor ($K = 0.94$), β is the full width

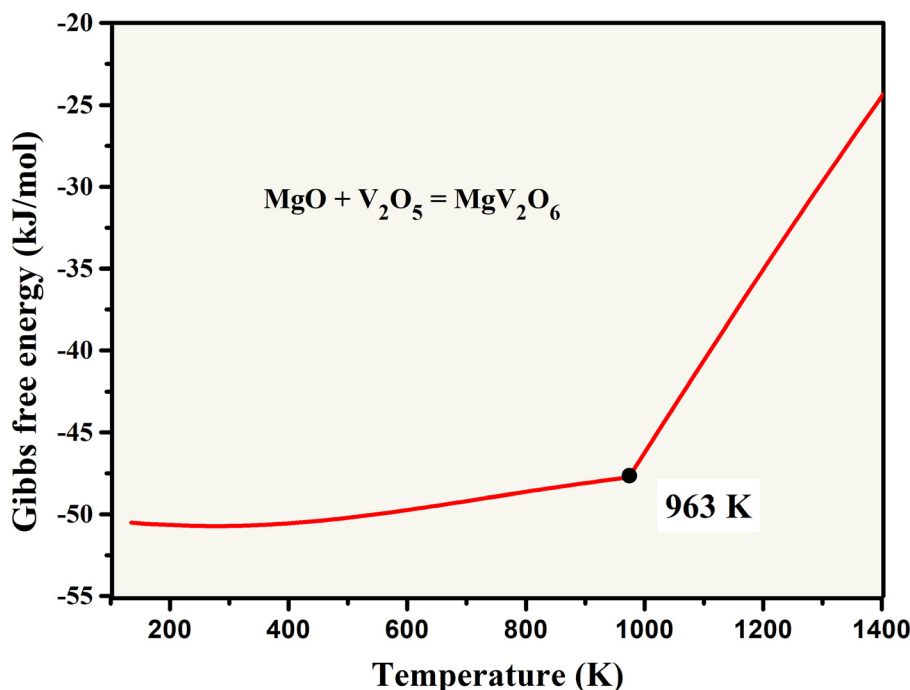


Fig. 1. Gibbs free energy for the MgV_2O_6 generation reaction.

Table 1

Thermodynamic data of the V_2O_5 , MgO , and MgV_2O_6 .

Compounds	$\Delta_f H_{298\text{ K}}^0$ ($\text{kJ}\cdot\text{mol}^{-1}$)	$S_{298\text{ K}}^0$ ($\text{J}\cdot\text{mol}^{-1}\cdot\text{K}^{-1}$)	C_p ($\text{J}\cdot\text{mol}^{-1}\cdot\text{K}^{-1}$)
V_2O_5	-1550590	130	$C_p(\text{v}_2\text{o}_5)=46.54-3.90 \times 10^{-3}T-13.22 \times 10^5T^{-2}$ (298-943 K)
MgO	-601500	27.9	$C_p(\text{m}_\text{g}\text{o})= 61.11-621154 \times 10^{-2}-296.20 \times 10^{-0.5}-5844612 \times 10^{-3}$ (298-3098 K)
MgV_2O_6	-2201658	160.7	$C_p(\text{m}_\text{g}\text{v}_2\text{o}_6)=C_p(\text{v}_2\text{o}_5)+C_p(\text{m}_\text{g}\text{o})$ (298-943 K)

at half maximum at the predominant (1 1 -1) peak position, and θ is the reflection angle of this height peak in radians. The mean crystallite size of MgV_2O_6 (74 nm) exceeded the parameters typical for nanoscale structures (20 nm).

Fig. 3 shows the FI-IR spectra of the MgV_2O_6 phase, which was calcinated at 873 K. It has been reported that the $\text{V}=\text{O}$ stretch in crystalline V_2O_5 gives rise to a sharp and intense band at 1020 cm^{-1} [31], while no obvious peaks at approximately 1020 cm^{-1} were found in this study. The band observed at 1629 cm^{-1} was assigned to absorb water. Strong bands at 495.7 , 815.9 , 1856.6 , 2924.1 , and 3415.8 cm^{-1} were found in the synthesized MgV_2O_6 . It can be seen that the spectrum of the synthesized samples corresponds with those previously reported for the same compounds.

The surface morphology of the MgV_2O_6 powder was further characterized by SEM, and characteristic micrographs were obtained at four different magnifications, namely, (a) $\times 800$, (b) $\times 3000$, (c) $\times 12,000$, and (d) $\times 24,000$, as shown in Fig. 4. The MgV_2O_6 powder consisted of rod- and belt-shaped particles. The smaller unshaped particles around the rod- and belt-shaped particles exhibited slight agglomeration due to the difference in growth velocities in different directions. The grain size can be estimated from the image in Fig. 4 (d) at $\times 24,000$ magnification. The particle size of MgV_2O_6 was estimated to be approximately 1–2 μm .

3.2. Solid-state phase transition

In a previous study, MgV_2O_6 was found to possess a temperature-dependent structural transformation at normal pressure, namely, α - MgV_2O_6 (brannerite type) and β - MgV_2O_6 (pseudobrannerite type), corresponding to low- and high-temperature phases, respectively.

Fig. 5 shows the DSC curve across the phase transition region at a specific heating rate of 10 K/min under an Ar atmosphere. Two obvious endothermic peaks are visible in the DSC curve, corresponding to the temperature-dependent solid-state phase transition and incongruent melting. The thermal fluctuations at approximately 773 K may be caused by noise and other operational errors, which did not affect the final results. The extrapolated onset temperature of the DSC curve was used in the present study. The experimental results demonstrated that the solid-state structural transformation of MgV_2O_6 occurs at approximately 841 K. The transition temperature of the solid phase transition was also reported by Mocała et al. [30] (808 K), Clark et al. [31] (840 K), and Cao et al. [32] (809 K). The present value is approximately 33 K higher than that reported by Mocała et al. [30] and 32 K higher than that reported by Cao et al. [32]. The purity and XRD patterns of the sample measured by Mocała et al. [30] were not mentioned, therefore, it may be not very accu-

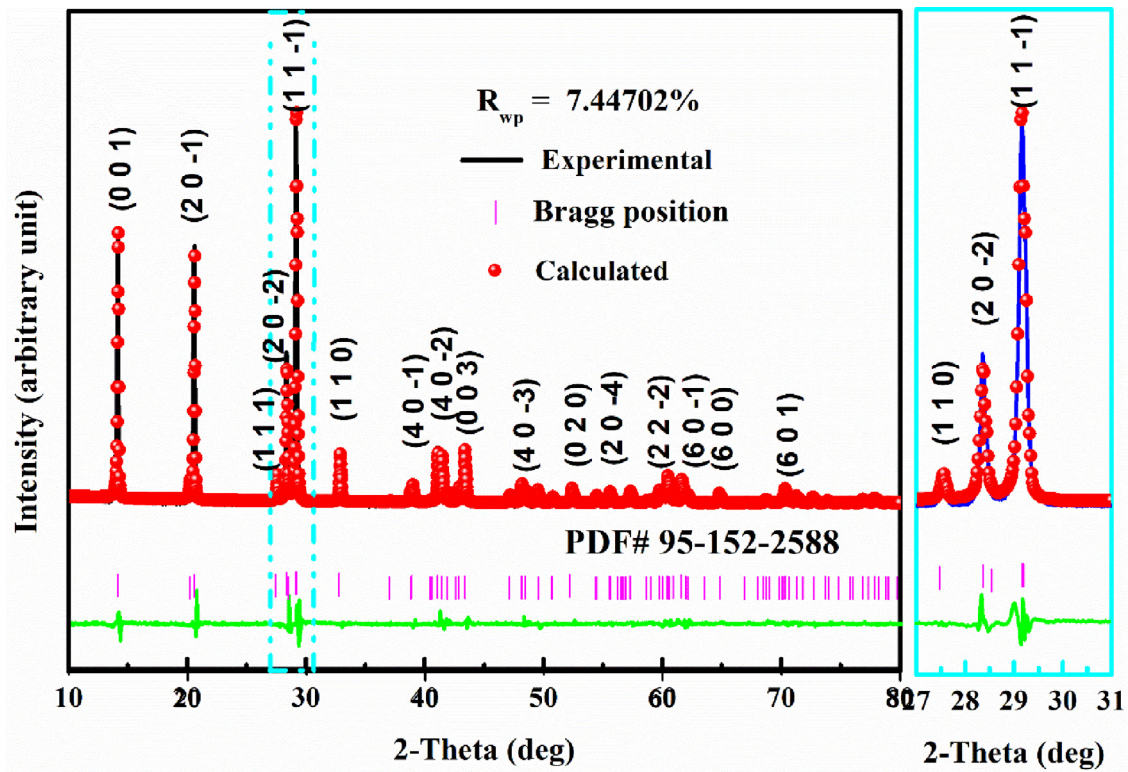


Fig. 2. XRD patterns and Rietveld refinement of the MgV_2O_6 sample by $Cu-K\alpha$ radiation at room temperature. The right side shows the enlarged view of the diffraction peak in the 2θ range of 27–31°.

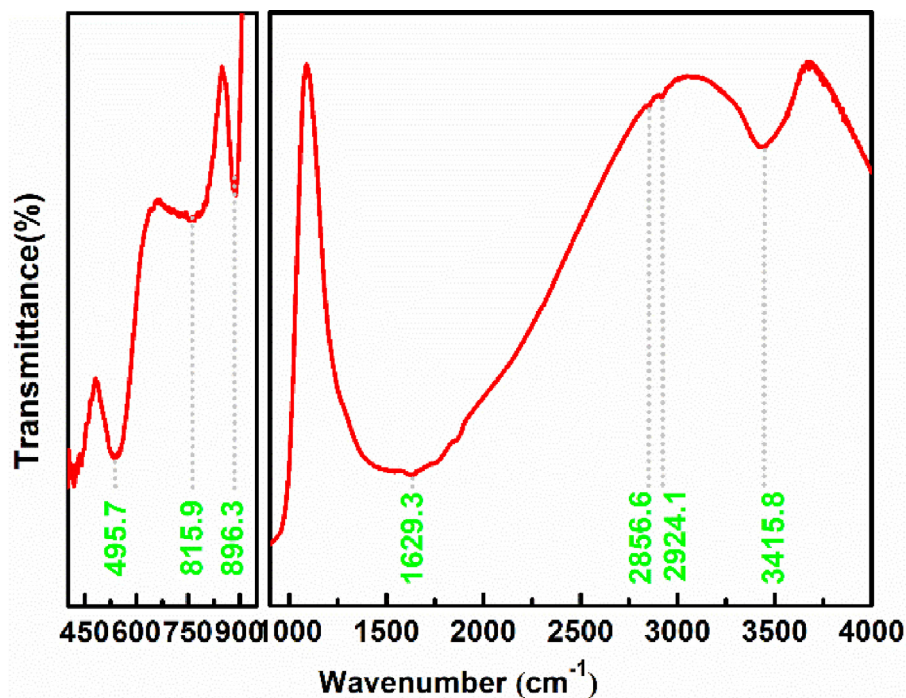
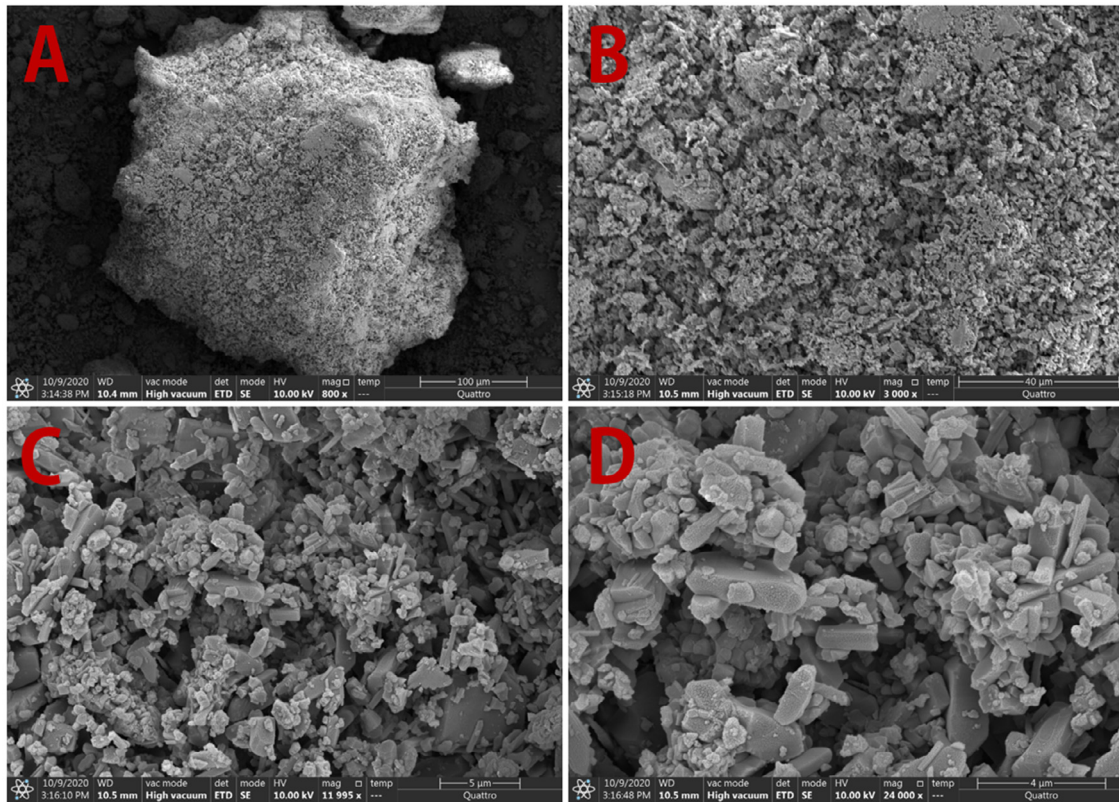
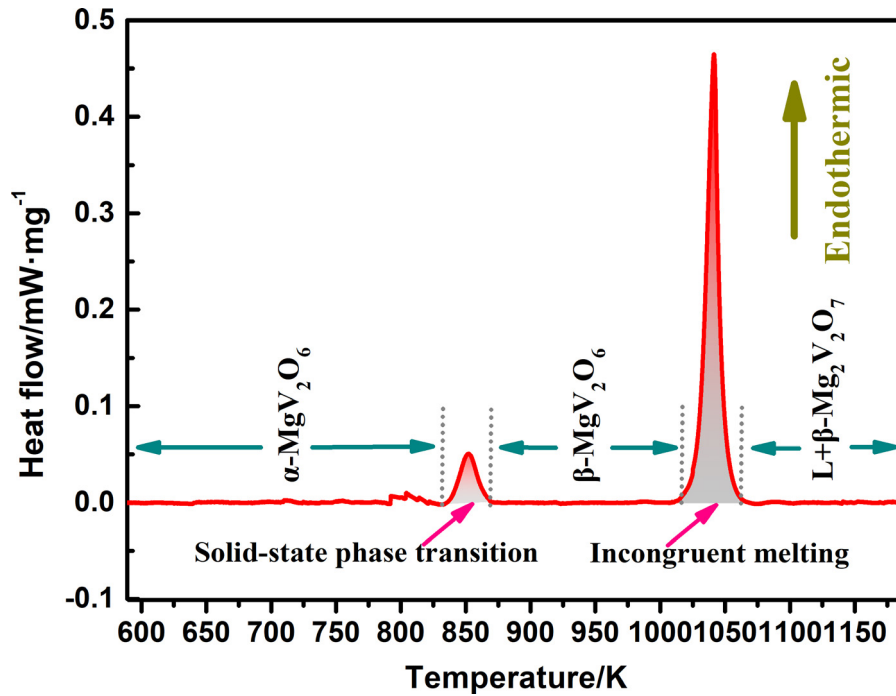


Fig. 3. FT-IR spectrum of the MgV_2O_6 sample.

Fig. 4. SEM images of the as-prepared MgV_2O_6 powder.Fig. 5. DSC curve of the as-prepared MgV_2O_6 powder.

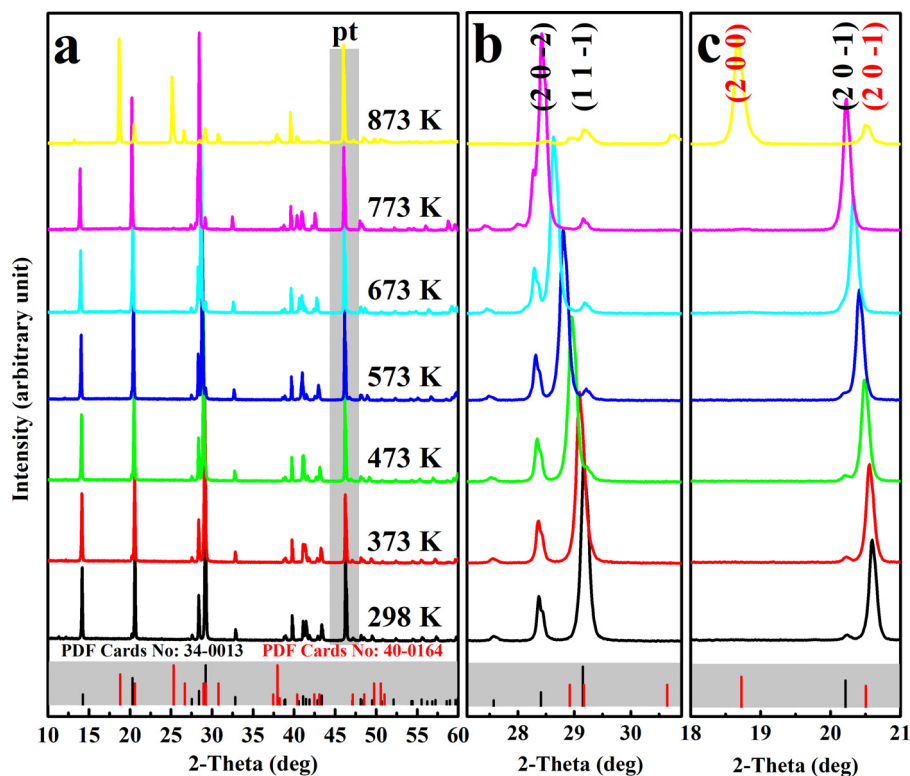


Fig. 6. XRD patterns of the MgV_2O_6 sample with Cu- $K\alpha$ radiation at high temperatures: (a) Full version in the 2θ range of $10\text{--}60^\circ$, (b) enlarged view of the diffraction peak in the 2θ range of $27\text{--}31^\circ$, and (c) enlarged view of the diffraction peak in the 2θ range of $18\text{--}21^\circ$.

Table 2

Phase transition type and temperature of MgV_2O_6 .

Phase transition type	Temperature/K	Refs.
Solid-state	808	Mocała et al. [30]
phase	840	Clark et al. [31]
transition	809	Clark et al. [31]
	841	This work
Incongruent	1015	Kerby et al. [33]
melting	1014	This work

rate. The phase transition temperature reported by Cao et al. [32] was obtained by optimizing the $\text{MgO-V}_2\text{O}_5$ phase diagram, which is not an experimental result. The present result is consistent with that reported by Clark et al. [31], and it was confirmed that the present result is more reliable and can be confidently used in the future. The experimental results from this study verified that incongruent melting occurs at approximately 1014 K, which is in agreement with the results of Kerby et al. [33], and the results are presented in Table 2. The enthalpy changes of the structural transition and incongruent melting were also determined by integrating the endothermic peaks in the DSC curve. The average values were 4.37 ± 0.04 kJ/mol and 26.54 ± 0.26 kJ/mol, respectively.

Fig. 6 (a) presents the XRD patterns of the MgV_2O_6 sample using Cu- $K\alpha$ radiation at 298, 373, 473, 573, 673, 773, and 873 K in the 2θ range of $10\text{--}60^\circ$. Fig. 6 (b and c) show an enlarged view of the diffraction peaks in the 2θ range of $27\text{--}31^\circ$ and $18\text{--}21^\circ$, respectively. The obvious diffraction

peak at approximately 44° is the platinum pattern, which does not affect the current diffraction results. The crystal structure of the prepared MgV_2O_6 was well matched with the standard card (ICDD card No: 95-152-2588) and did not change when the temperature was lower than 873 K; however, some slight differences were observed in the diffraction peak positions and intensities. In Fig. 6 (b), the position of the (1 1 -1) predominant peak at approximately 29.3° confirmed that the lattice parameters of the sample increased with an increasing temperature. The diffraction intensity of the (2 0 -2) peak remained almost unchanged, indicating no change in the spatial distribution of the crystallite orientations along the (2 0 -2) direction. The peak intensity and position variation tendency of another typical (2 0 -1) predominant peak were also similar to the (1 1 -1) peak. The diffraction patterns at 873 K were relatively different from the lower temperature version, where the peak position and intensity were reformed $\beta\text{-MgV}_2\text{O}_6$ is monocrystalline. The refinement of the cell parameters indicated that $\beta\text{-MgV}_2\text{O}_6$ was crystallized in a monoclinic system with space group $C2/m$, the lattice parameters of the MgV_2O_6 phase at various temperatures shown in Table 3, which exhibited anomalies associated with the structural phase transition, which strongly confirms the DSC results. Thermal expansion with an increasing temperature has a positive behavior and is accompanied by an increase in both the lattice parameters and cell volume. The phase transition in each case is followed by an approximate 14% increase in the unit cell volume, which is similar to the results of a previous study. The Clausius-

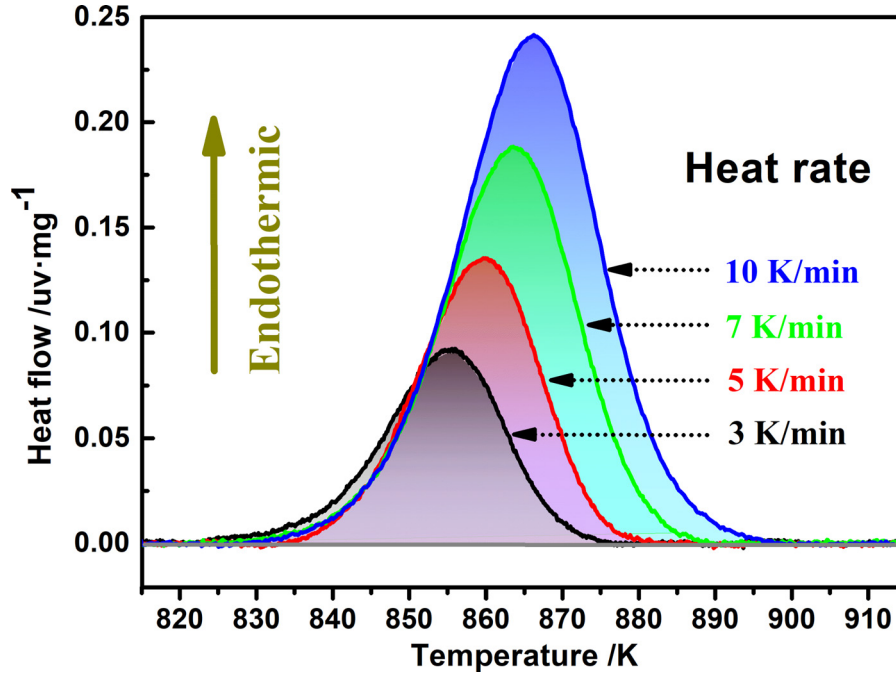
Fig. 7. Heat flow of the MgV₂O₆ sample with different heating rates.

Table 3

Unit cell parameter of the MgV₂O₆ at various temperatures.

	<i>a</i> (Å)	<i>b</i> (Å)	<i>c</i> (Å)	β (°)
298 K	9.280	3.501	6.731	111.76
373 K	9.302	3.501	6.740	111.45
473 K	9.321	3.500	6.749	111.13
573 K	9.339	3.500	6.762	110.80
673 K	9.359	3.499	6.773	110.49
773 K	9.382	3.499	6.781	110.39
873 K	9.695	3.573	6.854	102.28

Clapeyron relation can be described as:

$$\frac{dp}{dT} = \frac{\Delta_{\alpha}^{\beta} H_m}{TV_{\alpha}^{\beta} H_m} \quad (3)$$

where $\Delta_{\alpha}^{\beta} H_m$ and $\Delta_{\alpha}^{\beta} V_m$ are the enthalpy and volume changes before the phase transformation, respectively, and *T* is the structural transition temperature. As $\Delta_{\alpha}^{\beta} H_m > 0$ and $\Delta_{\alpha}^{\beta} V_m > 0$, a positive *dp/dT* slope is expected for the phase boundary, which means that the transformation temperature should not diminish with an increase in pressure.

Fig. 5 shows that the heat flow peaks of the solid-state phase transition did not interfere with the endothermic effect of fusion. Thus, a standard kinetic analysis can be applied to comprehensively explore the solid-state transition mechanism. The kinetics of the solid-solid phase transformation of the MgV₂O₆ were studied using the heating rates of 3, 5, 7, and 10 K/min. Fig. 7 shows the enlarged experimental DSC curves for the various heating rates. It is clear that the peak area of the solid-solid phase transition increased with an increased heating rate, and the peak of several heat flows slightly moved to the high-temperature zone, which occurs owing to thermal hysteresis. But the enthalpy change with various heating rates

Table 4

Avrami parameters *n* and *Kc* for the solid-solid phase transformation modification change of MgV₂O₆.

β (K/min)	<i>n</i>	<i>Kc</i>	<i>R</i> ²
3	1.70	1.33	0.99
5	3.44	1.00	0.99
7	3.67	0.32	0.99
10	3.73	0.14	0.99

is constant. The initial temperature of the DSC curves was almost stable, and it did not change with the heating rate, revealing that the temperature of the specific solid-state phase transition is constant during the heating process.

Fig. 8 shows the conversion ratio (α) curves for the various heating rates, demonstrating that the transition time was significantly decreased with an increased heating rate. The reaction mechanism can be further deduced by plotting $\ln[-\ln(1-\alpha)]$ against $\ln t$ according to the ln-ln method, as shown in Eq. (4):

$$\ln[-\ln(1-\alpha)] = n \ln t + \ln K. \quad (4)$$

$\ln K$ was modified by Jeziornig [34] when the ln-ln method was applied to isothermal solid-state phase transition and shows in Eq. (5):

$$\ln Kc = \frac{\ln K}{|\beta|} \quad (5)$$

The fitted parameters of the phase transitions are listed in Table 4. The value of *n* for the phase transition of MgV₂O₆ was relatively different, corresponding to the various heating rates. The *n* values were 1–2 when the heating rate was 3 K/min, which indicates that the transformation is controlled by a fibril-like (one-dimensional) mechanism. The *n* values were 3–4 when the heating rates were 5, 7,

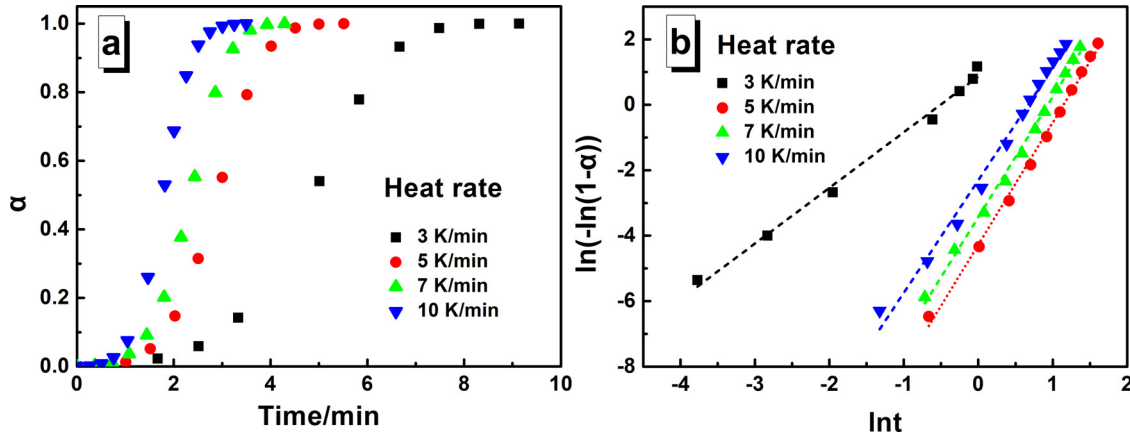


Fig. 8. Plot of $\ln[-\ln(1-X(t))]$ against $\ln t$ based on the Avrami model for the solid-solid phase transformation modification change of MgV_2O_6 .

and 10 K/min, which indicates that the transition was controlled by a spherulitic-type (three-dimensional) mechanism. This finding indicates that the solid-solid phase transition of MgV_2O_6 is controlled first by a fibril-like mechanism and then by a spherulitic-type mechanism with an increasing heating rate.

3.3. High-temperature thermodynamic properties of MgV_2O_6

The heat capacity of materials at high temperatures is a fundamental and essential thermophysical property and is indispensable for calculating chemical reactions, multi-phase equilibrium, and stability. Reliable experimental values are still absent in the literature and need to be measured using a calorimetric method.

In this study, the heat capacity of MgV_2O_6 at high temperatures was precisely determined by isothermal drop calorimetry. Fig. 9 shows the average sensitivity of the calorimetry obtained for each measuring sequence. The results indicate that the sensitivity remarkably increased with an increasing temperature, which is consistent with the results of Benes et al. [35]. However, because small heat contents are determined by the small temperature increase of the dropped sample, the enthalpy error for this temperature range on the absolute scale was acceptable, and the experimental data was also reliable.

In each experimental run, at least four drops of the sample pellets and four drops of the sapphires were prepared to eliminate experimental errors. Fig. 10 presents the typical heat flow curves for the eight drop tests at 923 K conducted in this study, where the blue line denotes the endothermic peak for the sapphire reference pellets, while the green line shows the endothermic peak for the MgV_2O_6 pellets. Each peak of the heat flow signal was then individually integrated to obtain the heat content before and after the dropping process. Then, the heat contents of the various experimental runs were used to calculate the enthalpy increments of the sample.

All the experimental results are listed in Table 5. The enthalpy changes of the solid-state phase transition (4.37 ± 0.04 kJ/mol) were subtracted when computing the enthalpy increments of the sample above 873 K to fit the

Table 5

Enthalpy changes of MgV_2O_6 sample, obtained by drop calorimetry at 1 atm.

T/K	ΔT 298.15 H_m /(J·mol ⁻¹)	T/K	ΔT 298.15 H_m /(J·mol ⁻¹)
573	89445.0	773	149075.3
623	104352.5	823	163982.5
673	119260.0	873	178890.2
723	134167.5	923	193797.5

experimental data as a single expression. All experimentally determined values were fitted by a least-squares method using the Maier-Kelley polynomial [36]:

$$\Delta H = aT + b/2T^2 - cT^{-1} + d \text{ (J} \cdot \text{mol}^{-1}) \quad (6)$$

where a ($=208.3$), b ($=0.03583$), c ($=-4809000$), and d ($=58430$) are the parameters:

The heat capacity equals the enthalpy variation divided by the temperature variation in the temperature range of 298–923 K using the fitted enthalpy variation equations. The corresponding standard C_p variation was then obtained by:

$$C_p = 196.95837 + 0.07007T - 1576740T^{-2} \text{ (298 - 973K)} \text{ (J} \cdot \text{mol}^{-1} \cdot \text{K}^{-1}) \quad (7)$$

The heat capacity of MgV_2O_6 was obtained by considering all the measured data present in Fig. 11. As previously mentioned, Khodos et al. [22] experimentally determined the heat capacity of MgV_2O_6 at 298.15 K as 164.8 ± 1.6 J mol⁻¹ K⁻¹. The temperature dependence of the heat capacity at high temperatures was also estimated by the Neumann-Kopp rule based on the addition of standard heat capacity of the simple oxide of MgO and V₂O₅, both of which were derived in literature. The estimated C_p value at 298.15 K was slightly higher than those obtained experimentally by Khodos et al., and they significantly increased with temperature when the temperature exceeded 673 K. A similar behavior was also observed in our previous study. In several other studies, the Neumann-Kopp rule yielded a significantly higher error at high temperatures for the mixed metal oxides. This can be explained by the difference in the cubic lattice crystal structure of MgO and the rhombus structure V₂O₅, while MgV_2O_6

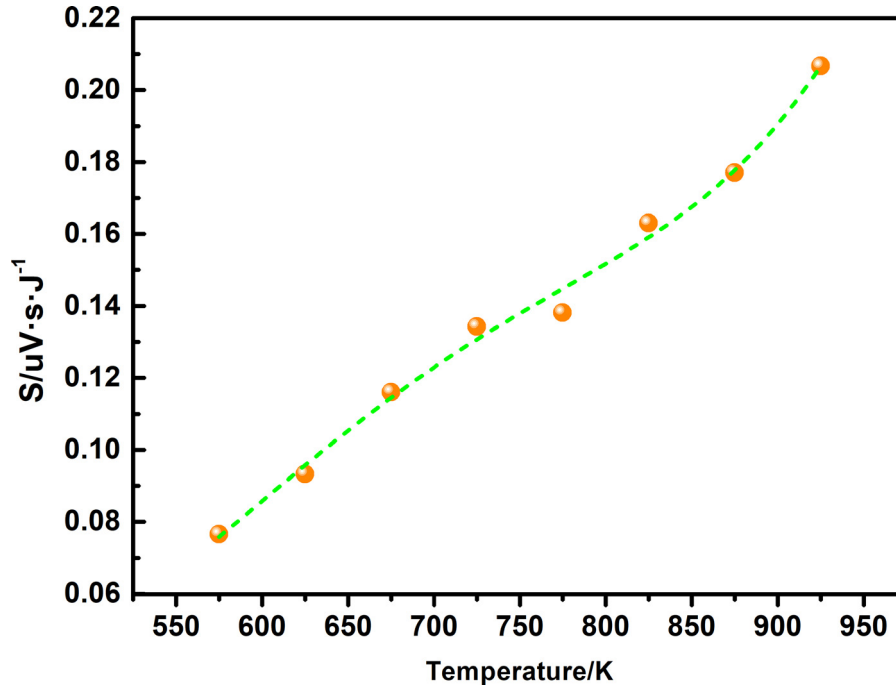


Fig. 9. The average sensitivity of the drop calorimetry determined in this study.

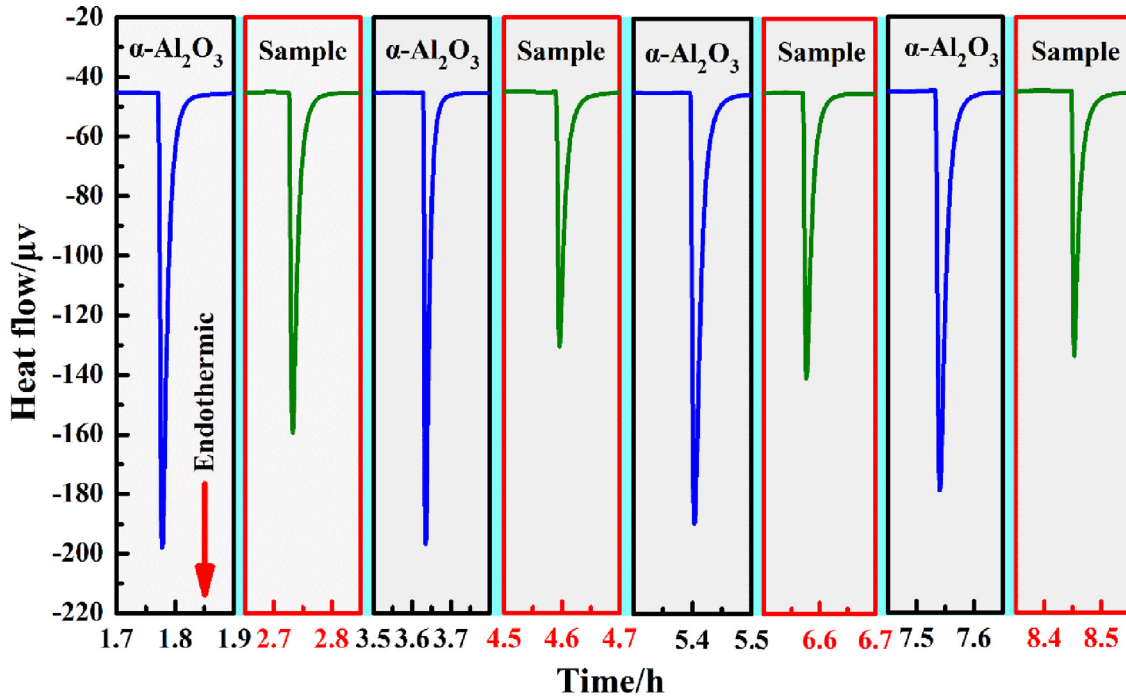


Fig. 10. Heat flow curves were obtained by drop calorimetry at 923 K.

crystallizes in a monoclinic system. Consequently, the predicted values based on the Neumann-Kopp rule, especially in the high-temperature region, are not sufficiently reliable and should be carefully considered during scientific research and industrial production. The experimental values based on the calorimetric method in this study can be used with confidence.

Based on the obtained heat capacity, the Gibbs free energy of the MgV₂O₆ can be calculated.

$$G_T^0 = \Delta_f H_{298 K}^0 + \int_{298}^T C_p dT - T \left[S_{298 K}^0 + \int_{298.15}^T \frac{C_p}{T} dT \right] \quad (8)$$

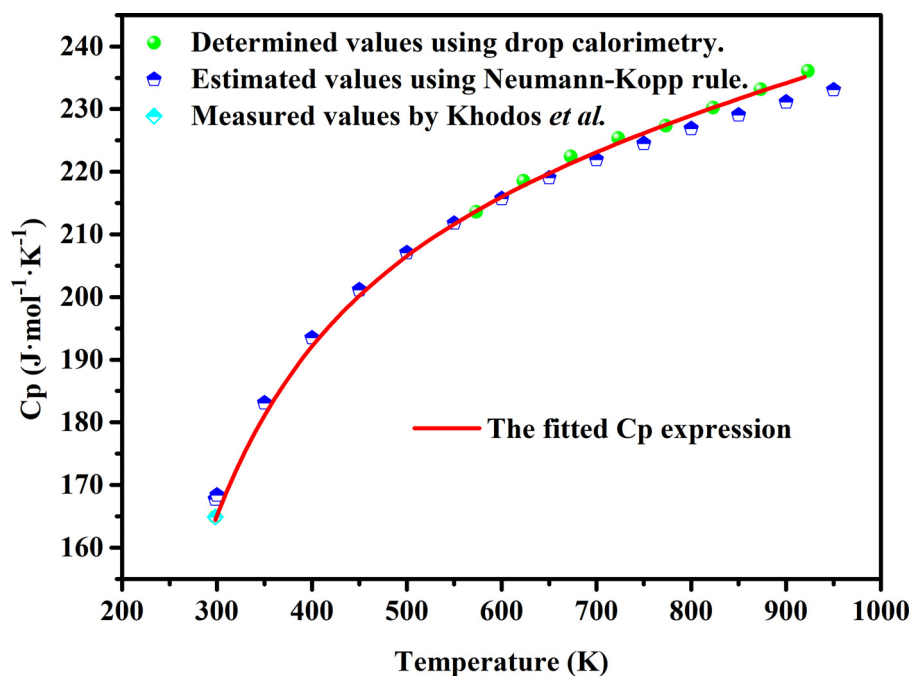


Fig. 11. Molar heat capacity of the MgV_2O_6 powder, for temperature in the 298–923 K range.

where $\Delta_f H_{298\text{K}}^0$ and $S_{298\text{K}}^0$ is the standard enthalpy of formation, and entropy at 298.15 K, C_p is the fitted high-temperature heat capacity, T is the absolute temperature.

4. Conclusion

MgV_2O_6 powder was obtained by facile solid-state sintering, and the crystal structure, phase transitions, and high-temperature thermodynamic properties were studied. The following conclusions were obtained from the results:

1. MgV_2O_6 crystallizes in a monoclinic system with the space group $C2/m$ and the room temperature lattice parameters of $a = 9.280 \text{ \AA}$, $b = 3.501 \text{ \AA}$, $c = 6.731 \text{ \AA}$, $\beta = 111.76^\circ$. The thermal expansion with increasing temperature has a positive behavior and is accompanied by an increase in the lattice parameters.
2. The phase transition enthalpy changes were determined by DSC as $\Delta H_1 = 4.37 \pm 0.04 \text{ kJ mol}^{-1}$ and $\Delta H_2 = 26.54 \pm 0.26 \text{ kJ mol}^{-1}$, corresponding to $\alpha\text{-MgV}_2\text{O}_6 \leftrightarrow \beta\text{-MgV}_2\text{O}_6$ at 841 K and the incongruent melting at 1014 K, respectively. The solid phase transition mechanism of MgV_2O_6 was further identified, indicating that the phase transition is controlled first by a fibril-like mechanism and then by a spherulitic-type mechanism with an increasing heating rate.
3. The heat capacity of MgV_2O_6 at 298–923 K was experimentally measured by drop calorimetry and was modeled as $C_p = 208.3 + 0.03583T - 4809000T^{-2}$ (298–923 K) ($\text{J}\cdot\text{mol}^{-1}\cdot\text{K}^{-1}$).

Acknowledgments

This work was supported by the National Key R&D Program of China (2018YFC1900500), and the Graduate Scientific Research and Innovation Foundation of Chongqing, China (Grant No. CYB20002).

References

- [1] J.B. Goodenough, Y. Kim, Chem. Mater. 22 (3) (2010) 587–603, doi:10.1021/cm901452z.
- [2] Z. Ding, Z. Chen, T. Ma, C.T. Lu, W. Ma, L. Shaw, Energy Storage Mater. 27 (2020) 466–477, doi:10.1016/j.ensm.2019.12.010.
- [3] Z. Ding, H. Li, L. Shaw, Chem. Eng. J. 385 (2020) 123856, doi:10.1016/j.ccej.2019.123856.
- [4] Z. Ding, Y. Lu, L. Li, L. Shaw, Energy Storage Mater. 20 (2019) 24–35, doi:10.1016/j.ensm.2019.04.025.
- [5] J. Jiang, Y. Li, J. Liu, X. Huang, Nanoscale 3 (1) (2011) 45–58, doi:10.1039/C0NR00472C.
- [6] P. Sun, P. Bai, Z. Chen, H. Su, J. Yang, K. Xu, Y. Xu, Small 16 (3) (2020) 1906462, doi:10.1002/sml.201906462.
- [7] F. Tong, S. Wei, X. Chen, W. Gao, J. Magnes. Alloy. 9 (6) (2021) 1861–1883, doi:10.1016/j.jma.2021.04.011.
- [8] D. Li, Y. Yuan, J. Liu, M. Fichtner, F. Pan, J. Magnes. Alloy. 8 (4) (2020) 963–979, doi:10.1016/j.jma.2020.09.017.
- [9] M. Rashad, S.D.A. Zaidi, M. Asif, J. Magnes. Alloy. 8 (4) (2020) 980–988, doi:10.1016/j.jma.2020.05.016.
- [10] M. Rashad, M. Asif, I. Ahmed, Z. He, L. Yin, Z.X. Wei, Y. Wang, J. Magnes. Alloy. 8 (2) (2020) 364–373, doi:10.1016/j.jma.2019.09.010.
- [11] Y. Yang, X. Xiong, J. Chen, X. Peng, D. Chen, F. Pan, J. Magnes. Alloy. 9 (3) (2021) 705–747, doi:10.1016/j.jma.2021.04.001.
- [12] Q. Li, X. Peng, F. Pan, J. Magnes. Alloy. 9 (6) (2021) 2223–2224, doi:10.1016/j.jma.2021.11.003.
- [13] S.V.S. Prasad, S.B. Prasad, K. Verma, R.K. Mishra, V. Kumar, S. Singh, J. Magnes. Alloy. 10 (1) (2022) 1–61, doi:10.1016/j.jma.2021.05.012.

- [14] C. Lu, H. Liu, L. Xu, H. Luo, S. He, X. Duan, X. Huang, X. Wang, Z. Lan, J. Guo, J. Magnes. Alloy. (2021), doi:10.1016/j.jma.2021.03.030.
- [15] X. Wu, Y. Dou, R. Lian, Y. Wang, Y. Wei, Energy Storage Mater. 48 (2022) 344–355, doi:10.1016/j.ensm.2022.03.039.
- [16] X. Wang, Z. Zhang, S. Xiong, F. Tian, Z. Feng, Y. Jia, J. Feng, B. Xi, Small 17 (20) (2021) 2100318, doi:10.1002/sml.202100318.
- [17] G. Pei, J. Xiang, L. Yang, X. Lv, Calphad 74 (2021) 102295, doi:10.1016/j.calphad.2021.102295.
- [18] D. Zhao, Y. Weijie, H. Kaifu, S.J. Leon, Progress Chem. 33 (9) (2021) 1586, doi:10.7536/PC200831.
- [19] M. Gondrand, A. Collomb, J. Joubert, R.D. Shannon, J. Solid State Chem. 11 (1) (1974) 1–9, doi:10.1016/0022-4596(74)90139-X.
- [20] T. Rui-Lian, L. Yan, T. Qiang, L. Na-Na, L. Hui, H. Dan-Dan, Z. Pin-Wen, W. Xin, Chin. Phys. B 22 (6) (2013) 066202, doi:10.1088/1674-1056/22/6/066202.
- [21] M.A. Rahman, M.A.R. Sarker, J. Alloy. Compd. 797 (2019) 630–639, doi:10.1016/j.jallcom.2019.05.081.
- [22] M.Y. Khodos, V. Zhuravlev, A.J.I.M. Fotiev, Inorg. Mater 15 (1) (1979) 98–99.
- [23] J. Leitner, P. Voňka, D. Sedmidubský, P. Svoboda, Thermochim. Acta 497 (1-2) (2010) 7–13, doi:10.1016/j.tca.2009.08.002.
- [24] J. Leitner, P. Chuchvalec, D. Sedmidubský, A. Strejce, P. Abrman, Thermochim. Acta 395 (1-2) (2002) 27–46, doi:10.1016/S0040-6031(02)00177-6.
- [25] G. Pei, J. Xiang, L. Yang, X. Jin, X. Lv, Calphad 70 (2020) 101802, doi:10.1016/j.calphad.2020.101802.
- [26] G. Pei, J. Xiang, X. Lv, G. Li, S. Wu, D. Zhong, W. Lv, J. Alloy. Compd. 794 (2019) 465–472, doi:10.1016/j.jallcom.2019.04.186.
- [27] D. Ditmars, S. Ishihara, S. Chang, G. Bernstein, E.D. West, J. Res. Natl. Bur. Stand. 87 (2) (1982) 159.
- [28] D.R. Stull, JANAF Thermochemical Tables, Clgh (1965).
- [29] V. Guskov, A. Khoroshilov, M. Ryumin, O. Kondrat'eva, A. Guskov, K.S. Gavrichev, Ceram. Int. 46 (4) (2020) 5402–5406, doi:10.1016/j.ceramint.2019.10.296.
- [30] K. Mocała, J. Ziółkowski, J. Solid State Chem. 69 (2) (1987) 299–311, doi:10.1016/0022-4596(87)90087-9.
- [31] G.M. Clark, R. Morley, J. Solid State Chem. 16 (3) (1976) 429–435, doi:10.1016/0022-4596(76)90060-8.
- [32] Z. Cao, N. Wang, W. Xie, Z. Qiao, I.H. Jung, Calphad 56 (2017) 72–79, doi:10.1016/j.calphad.2016.12.001.
- [33] R.C. Kerby, J.R. Wilson, Can. J. Chem. 51 (7) (1973) 1032–1040.
- [34] A. Jeziorny, Polymer 19 (10) (1978) 1142–1144, doi:10.1016/0032-3861(78)90060-5.
- [35] O. Beneš, P. Gotcu-Freis, F. Schwörer, R. Konings, T. Fanghänel, J. Chem. Thermodyn. 43 (5) (2011) 651–655, doi:10.1016/j.jct.2010.11.010.
- [36] C.G. Maier, K.K. Kelley, J. Am. Chem. Soc. 54 (8) (1932) 3243–3246.